JACS Au
AN OPEN ACCESS JOURNAL OF THE AMERICAN CHEMICAL SOCIETY

pubs.acs.org/jacsau

Article

Excited-State Dynamics of Crossing-Controlled Energy Transfer in Europium Complexes

Liangliang Wu, Yu Fang, Wanlong Zuo, Juanjuan Wang, Ju Wang, Shufeng Wang, Zhifeng Cui, Weihai Fang, Hao-Ling Sun,* Yunliang Li,* and Xuebo Chen*

Cite This: *JACS Au* 2022, 2, 853–864

Read Online

ACCESS | Metrics & More | Article Recommendations | Supporting Information

ABSTRACT: Photosensitized energy transfer (EnT) phenomena occur frequently in a variety of photophysical and photochemical processes and have traditionally been treated with the donor–acceptor distance-dependent Förster and Dexter models. However, incorrect arguments and formulae were employed by ignoring energy resonance conditions and the selection rules of the state-to-state transition in special cases, especially for the sensitive intramolecular EnT of lanthanide complexes. Herein, we proposed an innovative model of energy-degeneracy-crossing-controlled EnT, which can be experimentally confirmed by time-resolved two-dimensional photoluminescence measurements. The computationally determined energy resonance region provides the most effective channel to achieve metal-to-ligand EnT beyond the distance-dependent model and sensitively bifurcates into symmetry-allowed or -forbidden channels for some representative europium antenna complexes. The outcomes of the multidisciplinary treatment contribute to a complementary EnT model that can be tuned by introducing a phosphorescence modulator and altering the antenna-related parameters of the ligand-centered energy level of the $^3\pi\pi^*$ state and its spin–orbit coupling for the $^3\pi\pi^* \rightarrow S_0^*$ transition through mechanism-guided crystal engineering and should motivate further development of mechanistic models and applications.

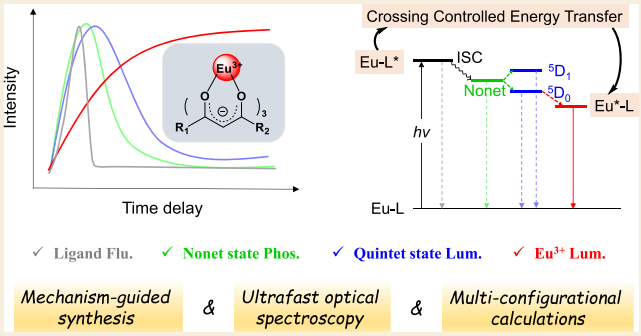

KEYWORDS: *photosensitization mechanism, resonant energy transfer, energy surface crossing, excited-state dynamics, ab initio calculation, time-resolved spectroscopy, crystal engineering*

Lanthanide complexes rely on metal-centered f–f luminescence to exhibit unique optical properties, such as sharp emission lines, long decay times, a large Stokes shift, a low autofluorescence background, and a high penetration depth.[1−15] These excellent properties are utilized to achieve the application of these complexes in a wide range of techniques, such as asymmetric catalysts,[1,2] upconversion nanoparticles,[3] functional materials,[4−9] and optical imaging agents.[10−15] Although most lanthanide ions are luminescent, the direct utilization of Ln-centered luminescence generally suffers from the low activation efficiency due to the forbidden electric-dipole f–f transition or the faint magnetic-dipole f–f excitation. However, perturbed by the ligand-field effect and spin–orbit interaction, the intraconfigurational electric-dipole transitions can be partly allowed.[16−18] The breakthrough study of sensitized intramolecular energy transfer (EnT) was conducted by Weissman[19] in 1942 and subsequently inspired researchers to seek suitable photoactive organic antennas that function as effective photosensitizers, achieving the light harvesting of lanthanide ions.[9,10,14,20−22]

Gaining a mechanistic understanding of lanthanide luminescence is challenging and encompasses the wide scope of photosensitized EnT related to the sensitization efficiency and the compromise between luminescence and quenching.[9,10,14,20−22] This intramolecular photosensitization is generally believed to be strongly distance-dependent from the ligand donor to the lanthanide acceptor (R_{DA}) and has traditionally been thought to proceed in the manners of Förster [with an $(R_{DA})^{-6}$ dependence], Dexter [with a distance dependence in $\exp(-\beta R_{DA})$], or dipole–multipole with distance dependences in $1/[(R_{DA})^{\lambda+2}]^2$ (λ = 2, 4, 6).[9,21,23,24] Electric dipole–quadrupole transitions are also parity-allowed, but they are weak and have been rarely identified unambiguously.[25] These weak interactions can be produced by using the mathematical treatment of the parity mixing with ligand-field perturbation. On the other hand, experiments with careful control were carried out to identify quadrupole

Received: December 29, 2021
Revised: March 8, 2022
Accepted: March 8, 2022
Published: March 16, 2022

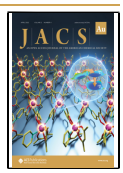

transitions in the solar absorption spectra.[26] However, experimental evidence has revealed that the quantum yields of lanthanide luminescence exhibit a sensitive fluctuation with the energy level of the ligand triplet state[27] and are significantly altered with coordination geometry even without apparent variations in the coordination bond length.[21,28] Spectroscopic studies have previously shown that the quantum yield of metal-centered luminescence is largely attributable to the sensitization efficiency, which itself is a product of ligand-centered intersystem crossing (ISC) and ligand-to-metal EnT.[29,30] Although time-resolved luminescence imaging and semi-empirical EnT rate estimations have been separately applied to a series of luminescent lanthanide probes,[31,32] a comprehensive understanding of the EnT mechanism of lanthanide complexes still lags behind. Ermolaev, Sveshnikova, and co-workers proposed the inductive-resonant theory to account for the nonradiative EnT from an electronically excited lanthanide ion to the surrounding molecular groups with the excitation of resonant vibrational states and made it possible to calculate the nonradiative transition rate constant.[33−35] In 1997, Horrocks *et al.* observed that a tryptophan antenna group efficiently sensitizes protein-bound Yb^{3+} over a distance of 8−11 Å under the excitation of a 290 nm UV light, causing it to emit near-infrared light at 977 nm.[36] From a formal point of view, this is a typical Förster EnT mechanism. Nevertheless, zero overlap between the emission spectrum of the tryptophan donor and the Yb^{3+} spectrum ruled out a Förster EnT and led the authors to propose an oxidation−reduction electron transfer mechanism involving ligand-to-metal charge-transfer excitation.[36,37]

Indeed, it was gradually recognized that the molecular mechanisms describing the lanthanide luminescence process remain poorly understood by using the current arguments and formulae.[38] Therefore, it is eagerly desired to develop an innovative model that provides the conceptual framework for identifying all possible determining factors, that is, the efficiency of ligand-centered ISC, the minimization of self-quenching luminescence, the ligand-to-metal EnT-mediated 4f electron redistribution, and the energy resonance conditions associated with selection rules aside from the donor−acceptor distance. As an important advancement toward this issue, in our group, a nonet−quintet state crossing was previously determined to govern the EnT through the rate-determining step of ligand-centered ISC concomitant with concerted 4f electron pairing on Eu^{3+} centers.[39] However, our model needs to pass the test of universality, impartiality, and rationality. Herein, we integrated high-level electronic structure calculations, photoluminescence-mechanism-based crystal engineering, and time-resolved spectroscopy to assign all transient and steady-state signals that are considered as the core issues for understanding complicated dynamics of lanthanide luminescence. These efforts aim to develop a universal theory for identifying the various spectral characteristics in the photoluminescence initiation, activation, deactivation, and treatment of photosensitized EnT. Thus, we can find feasible strategies to regulate ligand-centered ISC and the subsequent ligand-to-metal EnT rate. Moreover, the application scope of our model is required to be defined unambiguously, which facilitates the clarification of the relationship between our crossing-controlled model and the distance-dependent mechanism. Multidisciplinary perspectives in this work allow us to demonstrate some specific features of the dynamic control of photoluminescence and to provide a comprehensive understanding of crossing-controlled EnT for the photoactivated lanthanide complexes.

COMPUTATIONAL AND EXPERIMENTAL DETAILS

Ab Initio Calculations

In this work, the *ab initio* calculations of isolated antennas and their coordinated Eu(III) complexes were primarily performed at the CASSCF level of theory with the (12e/10o) and (12e/13o) active spaces, respectively. Based on the appropriate strategies of orbital localization and numerous computational tests, the selection criteria were adopted to make use of a balance model to describe the electron transitions in the specific chromophores of ligands and all configurations of 6f electrons in seven orbitals for the Eu^{3+} center (6e/7o). Energy-consistent scalar-relativistic Wood−Boring-adjusted 28-electron-core pseudopotentials were employed to account for the relativistic effects of Eu^{3+} and Br together with the corresponding basis sets.[40] The C, H, O, and N atoms were treated at the all-electron level with the 6-31G* basis set for the isolated antennas and the chromophores involved in primary light absorption and excitation transfer for the complexes **1**−**4**, while the remaining moieties were calculated by using the small basis set (STO-3G) to reduce the computational burden. All minima of the free antennas and complexes **1**−**4** in their singlet excited states (S_{CT} and $^1\pi\pi^*/^7F$) were obtained by full system state-averaged CASSCF optimizations using a two-root equally weighted approach, whereas a single-root optimization was adopted for the ground (S_0 and $S_0/^7F$) and triplet/nonet states (T_{CT} and $^3\pi\pi^*/^7F$) and the metal-centered quintet state ($S_0/^5D$). The minimum energy profiles of free antennas and the EnT of 1−4, as well as their radiative paths, were mapped by intrinsic reaction coordinate (IRC) computations to connect the above critical points. To consider the dynamic electron correlation effects, the single-point energies were recalculated at the CASPT2 level of theory based on the optimized structures of IRC/CASSCF computations. All CASSCF calculations, together with the IRC pathway for the isolated antennas were performed using the Gaussian 03 program package.[41] The CASPT2 and SO calculations for the free ligands and all computations for complexes **1**−**4** except the SO calculations using Molpro 2012[42] were carried out using the Molcas 8.0 program package.[43] More details are given in the Supporting Information.

Experimental Synthesis

The isolated antennas were synthesized *via* a routine preparation and separation procedure starting from commercially available reagents. A water solution of $Eu(Ac)_3{\cdot}6H_2O$ was used to form the coordinative bonds with 1-phenyl-3-pyridin-3-yl-propane-1,3-dione (PPPD), 1-(4-bromophenyl)-3-(pyridin-3-yl)propane-1,3-dione (*para*-Br-PPPD), and 1-(3-bromophenyl)-3-(pyridin-3-yl)propane-1,3-dione (*meta*-Br-PPPD) in a mixed solvent of an aqueous and nonaqueous (CH_3OH) matrix. The resulting solutions were stirred for several minutes, and then they underwent a series of solution transfer and filtration. Finally, the obtained solutions were left to evaporate at room temperature from several days to 1 month, eventually giving rise to the yellow crystals of complexes **1**−**4**. Detailed procedures can be found in the Supporting Information.

X-ray Crystallography and Physical Measurements

The intensity data for the crystals of **1**−**4** were collected using a Rigaku Super Nova, Dual, AtlasS2 diffractometer with graphite-monochromated Cu Kα radiation (1.54184 Å) at 100 K. All structures were solved using the olex2.solve structure solution program and further refined using the olex2.refine refinement package using Gauss−Newton minimization. All nonhydrogen atoms were refined anisotropically. Hydrogen atoms were placed at the calculation positions. Details of the crystal parameters together with the structural refinement of **1**−**4** are listed in Table S3, and selected bond lengths are given in Table S4. Elemental analyses of carbon, hydrogen, and nitrogen were carried out with an Elementar Vario EL analyzer. The FTIR spectra were recorded in the range of 4000−400 cm^{-1} using an AVATAR 360 Nicolet 380 FT/IR spectrometer using KBr pellets.

https://doi.org/10.1021/jacsau.1c00584
JACS Au 2022, 2, 853−864

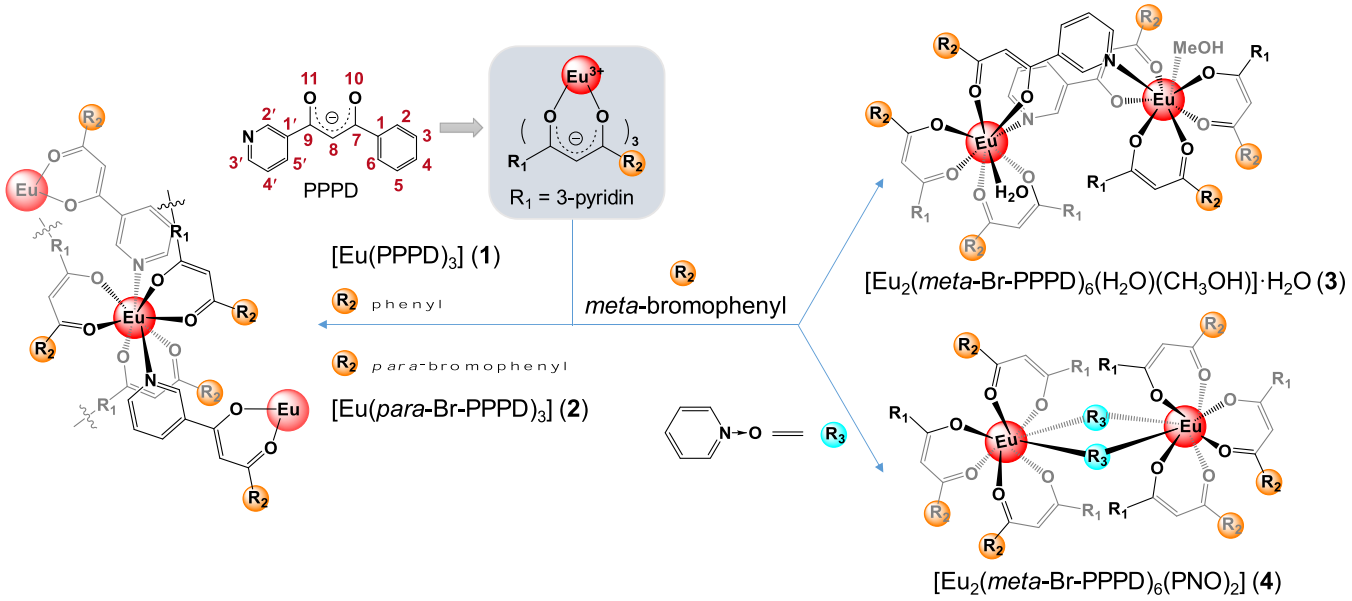

Figure 1. Coordination modes of β-diketone-chelated complexes **1**−**4**. Left panel, structures of complexes **1** and **2** formed with PPPD and *para*-Br-PPPD, respectively. Right panel, complexes **3** and **4** constructed by using *meta*-Br-PPPD. For complexes **1**−**4**, all the Eu^{3+} ions are octa-coordinated. For **1** and **2**, six oxygen atoms of diketone and two nitrogen atoms of pyridine are employed to form the O_6N_2 chemical environment. In the **3** and **4** dinuclear complexes, one or two nitrogen atoms of pyridine are substituted by the solvent molecules, resulting in the O_7N_1 and O_8 chemical environments, respectively.

Powder X-ray diffraction analyses were performed using a Rigaku Dmax-2000 X-ray diffractometer with Cu Kα (λ = 1.54059 Å) radiation. The luminescence spectra were recorded using an RF-5301PC spectrometer, and the emission quantum yields (the overall quantum yield, Φ_{QY}) were measured by using a HAMAMATSU Absolute PL Quantum Yield Spectrometer C11347 at room temperature.

Time-Resolved Luminescence Spectroscopy

The time-resolved luminescence spectra were collected using a commercial streak camera (Hamamatsu). In the system, a Ti:sapphire regenerative amplifier system produced a 90 fs laser pulse centered at 800 nm with a 3 mJ output energy at a 1 kHz repetition rate. The sample was agitated at 400 nm by doubling the 800 nm pulse using a beta barium borate crystal. The luminescence decay curve for each peak was plotted against the delay time and fitted in Figure 4a. The time-resolved and spectrally resolved luminescence images for each sample were recorded by averaging 100,000 laser shots and are shown in Figure 4b.

Transient Mid-IR Spectroscopy

The conformational changes and the energy relaxation dynamics in excited-states were investigated using a home-built ultrafast transient mid-IR system. In brief, the experimental setup consists of a Ti:sapphire regenerative amplifier (SpectraPhysics, Spitfire) seeded using a Ti:sapphire oscillator (Spectra Physics, Tsunami) to produce a 1 kHz train of 100 fs pulses centered at 800 nm with an average pulse power of 5 mJ. The corresponding output is split into two components, and 30% of the output power can be used to generate 400 nm pump pulses (*ca.* 100 μJ per pulse at the sample) *via* the second harmonic generation. The remaining 70% is employed to pump an automated optical parametric amplifier TOPAS (Spectra-Physic, Spitfire) to produce mid-IR probe pulses centered at 5 μm with a 350 cm^{-1} spectral width and 35 μJ output energy. The probe pulse and pump pulse were overlapped at the sample position with the spot sizes of 80 and 120 μm, respectively. The time delay between these two pulses was precisely regulated by a mechanical translation stage (IMS600LM, Newport). The produced signals were collected using a 64-channel detector (FPAS 0144 Infrared Systems Development) combined with a 300 mm focal-length spectrometer (Princeton Instruments 2300i).

RESULTS AND DISCUSSION

Photoluminescence-Mechanism-Based Crystal Engineering

Computational tests together with an extensive literature survey show that the β-diketone ligand class contains a negatively charged binding site to facilitate the formation of stable, neutral, 3:1 ligand−lanthanide luminescent complexes with the trivalent lanthanide cation (*i.e.*, Eu^{3+}). The CASPT2//CASSCF calculations demonstrate that the introduction of suitable electron acceptor groups in the β-diketone ligand instantaneously imposes a bright charge-transfer excitation state that results in electron promotion from the diketone center to substituted groups. By using the feasible approach of molecular engineering, the excitation energies of the ligand-centered bright state can be regulated to the appropriate resonance level, thereby sensitizing the lanthanide luminescence effectively.[44−48] Based on numerous test calculations, a pyridine ring was eventually selected as the electron-acceptor group for the photoinduced charge transfer (PICT) along the desired direction, which can be enhanced by the incorporation of an electron-donating group of the phenyl ring on the other side of the diketone center, resulting in the PPPD (Figure 1) antenna ligand. Benefiting from the ingeniously designed molecular skeleton bearing the enhanced PICT, the antenna ligand of PPPD exhibits strong absorption with a large oscillator strength (f = 0.47) over the visible-light range (λ_{max}: *ca.* 400 nm, Table S1). More importantly, the $^3\pi\pi^*$ triplet energy level of the PPPD ligand is computationally predicted to be 52.2 kcal mol^{-1} (18,270 cm^{-1}, Table S2) and is very close to the optimal 19,000 cm^{-1} above the ground-state $^7F_0$ of Eu^{3+}.[23,44] On the other hand, nine possible active sites can be present in the pyridine and phenyl rings of PPPD to tune the corresponding spin−orbit couplings (SOCs) for the $^3\pi\pi^* \rightarrow S_0$ transition of antenna ligands. Computational tests have demonstrated that the utilization of the heavy atom Br in

https://doi.org/10.1021/jacsau.1c00584
JACS Au 2022, 2, 853−864

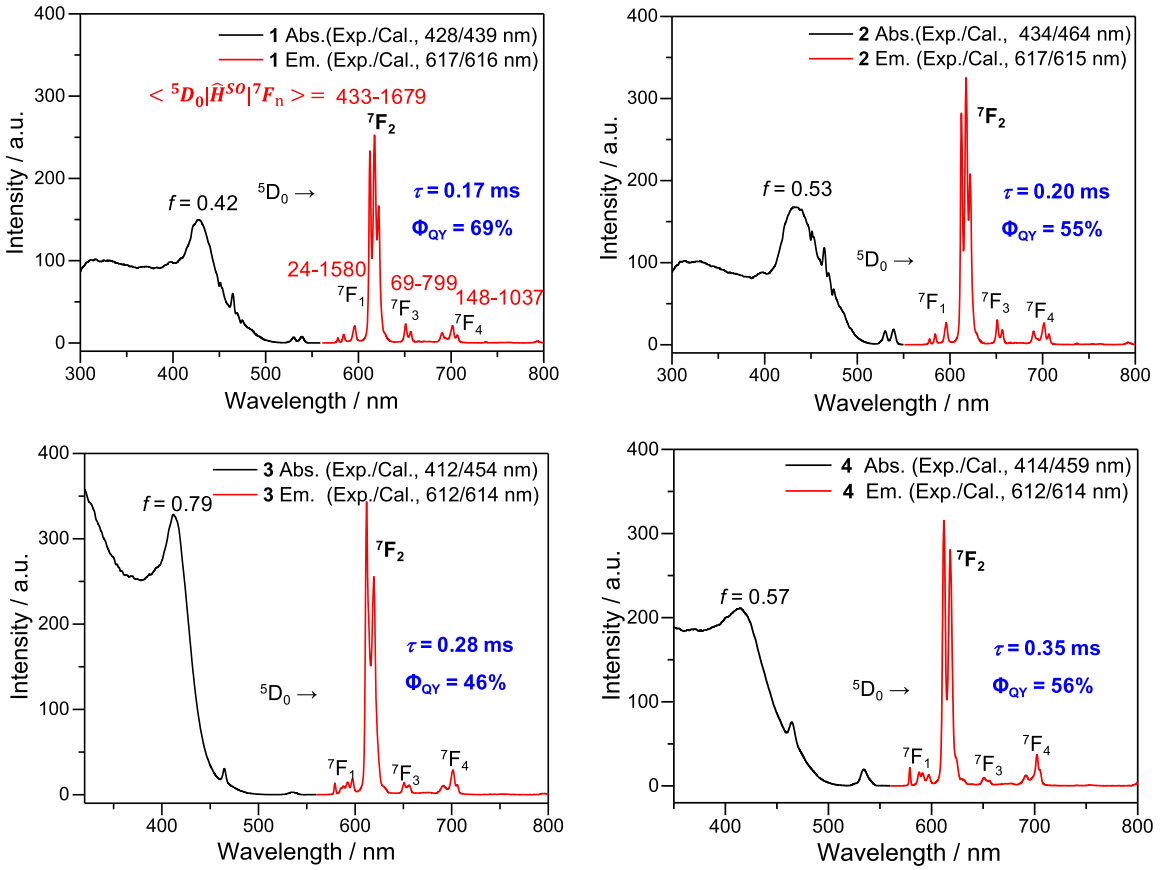

Figure 2. Photoluminescence properties of **1**−**4**. Visible-light absorption (black) and emission (red) spectra for **1**−**4**. The maximum absorption and the most relevant Eu(III) emission lines are theoretically assigned and labeled by calculating the vertical excitation energies (cal., nm) and oscillator strengths (*f*) of the intra-*β*-diketone ligand $S_0 \rightarrow S_{CT}(^1\pi\pi^*)$ transition, as well as the spin−orbit matrix elements (cm^{-1}) among the sublevels of the metal-centered $^5D_0 \rightarrow {}^7F_J$ (J = 1, 2, 3, 4) transitions. The overall photoluminescence quantum yield (Φ_{QY}) and lifetimes (τ, ms) are provided in blue for the europium(III) complexes of **1**−**4**.

the *meta*-position of the phenyl moiety (*i.e.*, 3-Br-PPPD) notably improves SOC but imposes a negligible influence on the triplet energy level of antenna ligands (Table S2). This implies that the *meta*-phenyl group may function as an ideal ligand-centered ISC moderator to cooperatively regulate the efficiencies of ligand-to-metal EnT associated with the photoluminescence of Eu^{3+}−diketonate complexes.

Following these valuable theoretical insights, we successfully synthesized the PPPD ligand and its *para*- and *meta*-bromine-substituted derivatives (*para*-Br-PPPD and *meta*-Br-PPPD). Careful crystal engineering was further performed by using the prepared ligands in a methanol solution with $Eu(Ac)_3{\cdot}6H_2O$ in a mixed solvent of CH_3OH and H_2O, eventually giving rise to bright yellow crystals of the Eu−PPPD (**1**), Eu−*para*-Br-PPPD (**2**), and Eu−*meta*-Br-PPPD (**3**) complexes (Figures 1 and S2). Single-crystal X-ray structure analyses reveal that both **1** and **2** crystallize in the orthorhombic space group *P*bcn and display an interesting two-dimensional (2D) layer structure sustained by the *meta*-pyridine nitrogen atoms of the PPPD ligands (Figures S3 and S4). The *β*-diketone parts of all three coordination PPPD ligands adopt bidentate chelating modes, whereas the *meta*-pyridine-N atoms of two PPPD ligands connect adjacent Eu^{3+} ions to form a 2D layer parallel to the *ab* plane, with the intralayer Eu···Eu distances from 8.2 to 9.4 Å. Unlike the spatial arrangement of **1** and **2**, the crystal structure of **3** undergoes a remarkable variation due to the squeezed coordination space in the presence of *meta*-bromine, in which one coordination site around the Eu^{3+} ion occupied by the *meta*-pyridine group is replaced with small molecules of water or methanol, forming a dinuclear structure of $[Eu_2(meta\text{-Br-PPPD})_6(H_2O)(CH_3OH)]{\cdot}H_2O$ (**3**) (Figure S5). To avoid a possible quenching effect from the O−H vibrations in H_2O/CH_3OH,[4,6−11,13−15,20−22] pyridine-*N*-oxide (PNO) ligands are employed to replace H_2O and MeOH, generating another dimeric complex of $Eu_2(meta\text{-Br-PPPD})_6(PNO)_2$ (**4**) connected by double PNO bridges.

Photoluminescence Performance of 1−4

The luminescence properties of **1**−**4** in their solid state were investigated experimentally at room temperature and theoretically assigned based on CASPT2//CASSCF computations. The decay curves of 550−750 nm emissions were recorded unambiguously upon visible-light irradiation at 410−440 nm (Figure S2). For all crystals, the decay curves were well fitted to a single-exponential function (Figure S7), which indicates that there exists a uniform coordination environment around the Eu^{3+} ion for each crystal. The computational results well reproduce the features of the experimental spectra, revealing that the antenna ligand-centered absorptions cause the PICT along a desired direction from diketone to pyridine moieties, which can be enhanced by the introduction of electron-donating Br atoms in the phenyl group. This accounts for a significant improvement in the intensity of optical absorption for bromine-substituted complexes **2**−**4** compared with that of **1** in the absence of Br, which is also confirmed by the

https://doi.org/10.1021/jacsau.1c00584
JACS Au 2022, 2, 853−864

Table 1. Kinetic Parameters for the Crossing-Controlled EnT of Complexes 1−4

	calculated by our crossing-controlled model			derived from experimental measurement					
complexes	$\langle {}^7F_0\|H^{SO}\|{}^5D_J\rangle$[a]	$\langle S_0\|H^{SO}\|{}^3\pi\pi^*\rangle$[a]	k_{ISC} ($10^6 s^{-1}$)[b]	τ_{EnT} (ns)[c]	τ (ms)	Φ_{QY}	k_{rad} (s^{-1})[d]	k_{nr} (s^{-1})[d]	η_{Eu}[d]
1	137−1515 ($^5D_1$)	0.2−0.8	2.6−41.0	12	0.17	0.69	983	4899	0.17
2	34−657 ($^5D_0$)	0.3−1.7	5.9−190.4	28	0.20	0.55	1013	3987	0.20
3	373−1444 ($^5D_1$)	0.3−1.9	5.7−229.4	6	0.28	0.46	883	2688	0.25
4	35−969 ($^5D_0$)	0.3−2.2	6.3−338.0	8	0.35	0.56	812	2045	0.28

[a]Spin−orbit matrix elements (SOMEs) of $\langle S_0|H^{SO}|{}^3\pi\pi^*\rangle$ and $\langle {}^7F_0|H^{SO}|{}^5D_J\rangle$ at NQC($T_1/{}^7F$−$S_0^*/{}^5D$) are provided in cm^{-1}, accounting for the ligand-centered ISC to the ground S_0 state and the metal-centered f electron pairing to the excited ^5D_J state, respectively. [b]Ligand-centered ISC (k_{ISC}) of $^3\pi\pi^* \rightarrow S_0^*$ is theoretically obtained based on the SOMEs of $\langle S_0|H^{SO}|{}^3\pi\pi^*\rangle$ and the corresponding energy gaps. [c]The durations (τ_{EnT}, ns) of EnT, which can be estimated by the delay time differences between the phosphorescent emission of the nonet state and the photoluminescence of the $^5D_0$ state at the NQC on the basis of time-resolved spectral data. [d]The rate constants of radiative/nonradiative relaxations (k_{rad}/k_{nr}, s^{-1}) and the metal radiative decay efficiencies (η_{Eu}) were calculated by using the experimentally recorded overall quantum yields (Φ_{QY}) and lifetimes (τ) based on the previously reported method.[52]

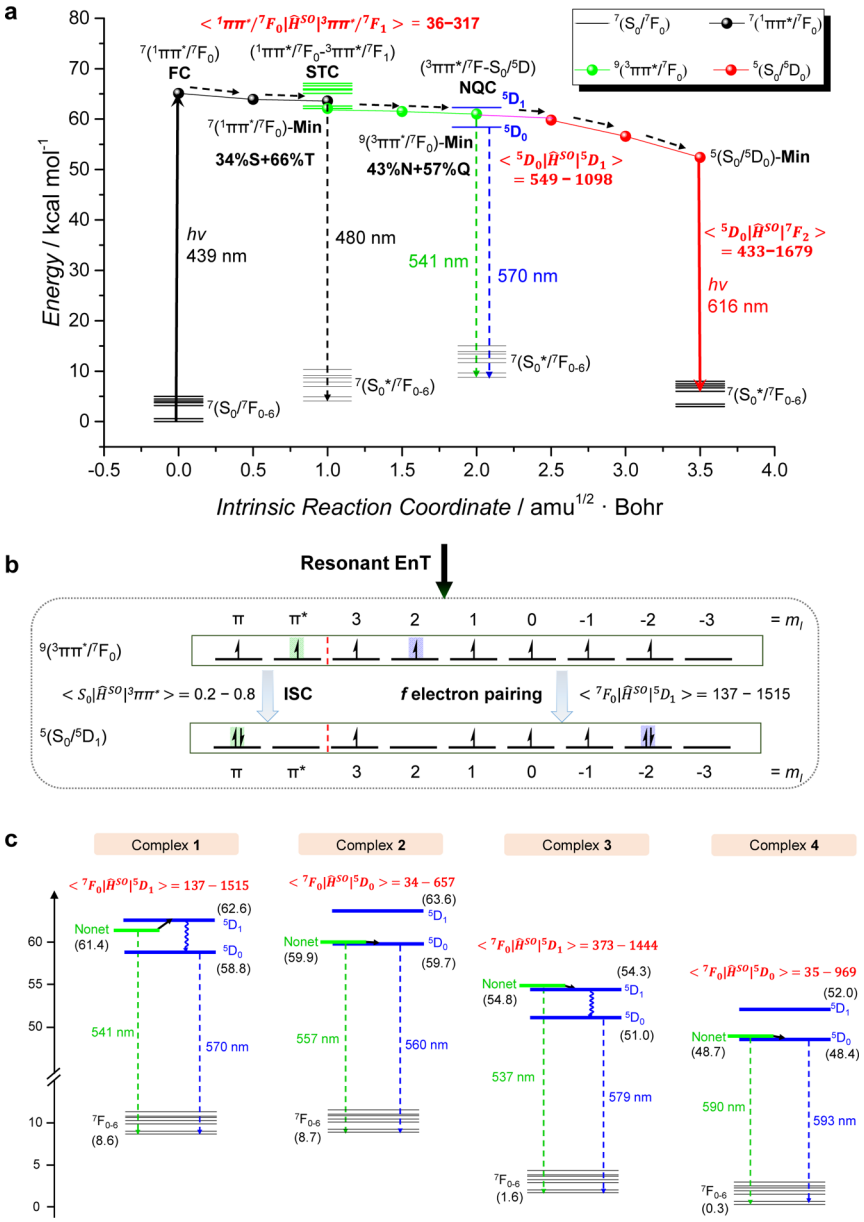

Figure 3. Crossing-controlled EnT and radiative paths of **1**−**4**. (a) Minimum-energy profiles for the crossing-controlled EnT of complex **1** obtained at the CASPT2//IRC//CASSCF level of theory. (b) Electron shift mode of EnT for **1**. (c) Energetic diagrams of the NQC region for **1**−**4**, with the relative energy of each state (in kcal mol^{-1}) given in parentheses. The SOCs between two specific states ψ_1 and ψ_2 ($\langle\psi_1|\tilde{H}^{SO}|\psi_2\rangle$) are given in cm^{-1} with an interval showing the minimum (nonvanishing) and maximum spin−orbit matrix elements.

https://doi.org/10.1021/jacsau.1c00584
JACS Au 2022, 2, 853−864

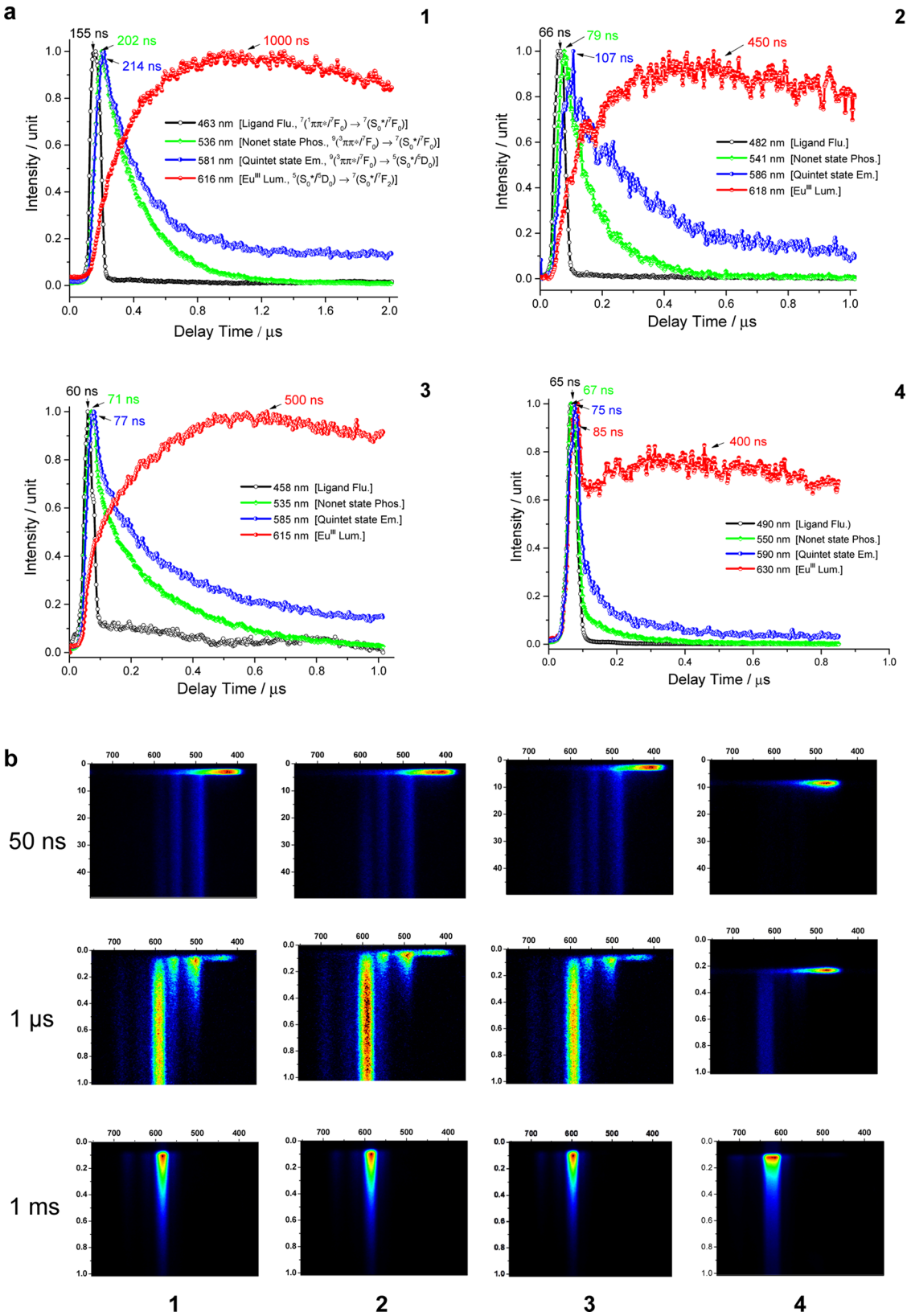

Figure 4. Excited-state dynamics of **1**−**4**. (a) Time-resolved luminescence spectra of **1**−**4** irradiated by visible light at 400 nm. The colored lines indicate the fittings to the dynamic data by using four exponential functions, which can be theoretically assigned to emissions from ligand-centered fluorescence (black), nonet-state phosphorescence (green), and the quintet-state (blue) and metal-centered (red) luminescence. (b) Time-resolved 2D photoluminescence spectra captured by a streak camera at the time delays of 50 ns, 1 μs, and 1 ms for samples **1**−**4**.

calculated oscillator strengths (f) for the *intra*-ligand CT $\pi\pi^*$ transitions of $S_0 \rightarrow S_{CT}(^1\pi\pi^*)$ (Table S7).

The visible-light absorption bands of **1**−**4** extend to the region of more than 500 nm and are seamlessly connected with

https://doi.org/10.1021/jacsau.1c00584
JACS Au 2022, 2, 853−864

the emission bands of metal-centered luminescence. Compared with the corresponding absorption spectra, the luminescence spectra of **1**−**4** exhibit more informative signals and originate from the lowest level of the excited quintet state ($^5D_0$) to the J levels of the septet ground state of ^7F_J (J = 0−6).[23,49,50] Unlike the tunable absorption spectra, the metal-centered emission spectra of **1**−**4** remain almost unchanged. Accurate calculations at the CASPT2//CASSCF level reveal that the f electron unpairing of $^5D_0 \rightarrow {}^7F_2$ takes place in a symmetry-allowed manner ($m_l = -2 \rightarrow m_l = +2$). The corresponding SOC upon ligand-field perturbation is predicted computationally to be 433−1679 cm^{-1} and is much larger than those for the assignable transitions of $^5D_0 \rightarrow {}^7F_J$ (J = 1, 3, 4) in the emission spectra of **1**−**4** (Figure 2 and Table S8). The present computational evidence reveals that the dominant $^5D_0 \rightarrow {}^7F_2$ transition peaking at 612−617 nm originates intrinsically from the strong coupling between the sublevel of quintet−septet states to contribute to the strengthened intensity of the favorable transition *via* symmetry-allowed f electron unpairing.

In addition to the absorption and emission spectra, the experimentally recorded overall quantum yields (Φ_{QY}), lifetimes (τ), calculated rate constants of radiative/nonradiative relaxations (k_{rad}/k_{nr}, s^{-1}), and metal radiative decay efficiency (η_{Eu}) serve as the key physical parameters to describe the photoluminescence properties of **1**−**4**. Parent complex **1** exhibits strong visible-light-sensitized luminescence with a high quantum yield (69%) and a moderate lifetime (0.17 ms). The quantum yield of **2** decreases sensitively to 55% but shows an increase in lifetime to 0.20 ms, although its crystal structure and coordination environment remain almost unchanged in comparison with the case of **1**. A relatively low quantum yield (46%) was found in the photoluminescence of **3** when the infinitely extended structure for **1** and **2** underwent dramatic structural deformation, generating a dimeric arrangement with a shortened Eu^{3+}−Eu^{3+} distance from *ca.* 9.3 Å (**1** and **2**) to 7.5 Å (**3**). As a consequence of the structural modification from the O_6N_2 chemical environment for **1** and **2** to O_7N_1 for **3**, the radiative/nonradiative rate constant (k_{rad}/k_{nr}) of **3** simultaneously shows a noticeable decrease compared with those of **1** and **2** (see Table 1). This quantum yield reduction was measured previously in the dimeric structure of the carbazole-based β-diketonate Eu^{3+} complex with respect to its mononuclear counterpart, which was roughly explained by the concentration quenching in the case of the closer Eu^{3+}−Eu^{3+} distance by neglecting the forbidden nature of $^5D_0 \rightarrow {}^7F_0$ transition.[51] In our case, the decreasing quantum yield of **3** mainly suffers from the nonradiative quenching by O−H vibrations in the presence of coordinated water/methanol around lanthanide ions, while possible vibronically assisted nonradiative deactivation cannot be excluded. This drawback is overcome by eliminating coordinated H_2O/CH_3OH *via* the introduction of the PNO solvent to improve the quantum yield (56%) of dimeric complex **4**. Consequently, the nonradiative rate for **4** (O_8 surroundings) is effectively suppressed, thereby giving rise to a 12% higher efficiency of metal radiative decay (η_{Eu}, 0.28) compared with **3** (0.25) by changing the coordinated solvent molecule to PNO. The lifetime of **4** increases doubly to 0.35 ms compared with that of **1** (0.17 ms), which is mainly attributed to the rigidity enhancement from **1** to **4**, thus largely shutting down the quenching channels *via* vibrations. Overall, the modification of the Eu chemical environment from the mixed O/N-donor to the fully O-donor atoms exhibits an increasing lifetime from 0.17 to 0.35 ms (see Table 1), which demonstrates an effective suppression of nonradiative decay, particularly from the Eu−O/N vibration deactivation. The present crystal samples exhibit diverse photoluminescence properties and different microcoordination environments around the Eu^{3+} metal, which provides a versatile platform for investigating the dynamic mechanisms of the visible-light-sensitized luminescence of europium complexes.

Dynamic Mechanisms of Crossing-Controlled EnT

To elucidate the dynamic events of photoluminescence, the minimum-energy profiles for the visible-light-initiated complexes **1**−**4** were first computed and summarized, as shown in Figure 3. These dynamic processes were further monitored by using transient luminescence spectra and are displayed in Figure 4. Visible-light irradiation instantaneously takes complexes to the bright spectroscopic septet state $^7(S_{CT}(^1\pi\pi^*)/{}^7F_0)$, which originates from the spin-allowed ligand-centered CT excitation but exhibits a more localized character than that of the isolated antenna ligand (Tables S1 and S7). Eu−O coordination imposes a structural constraint on the rotational deformation of pyridine or benzene rings along the C−C bond of the diketone plane that is mainly responsible for the nonradiative decay of visible-light-irradiated free antenna ligands (Figure S1). As a consequence, the ligand-centered radiative channels for the Eu−O coordinated complexes open and thus give rise to ligand-centered luminescence (cal. 480 nm for **1**) at the minimum of the bright septet state of $^7(^1\pi\pi^*/{}^7F_0)$−Min. Consistently, the first intermediate state with a noticeable band at 463 nm was observed at a time delay of 155 ns in four componential time-resolved luminescence spectra of **1** (Figure 4a). Careful energy analyses and SOC calculations reveal that the presence of relativistic effects and coordinative constraints resulting from the heavy Eu^{3+} atom causes a significant increase in the spin−orbit interaction of the complexes among singlet−triplet states, that is, coupling between $^7(^1\pi\pi^*/{}^7F_0) \rightarrow$ and $^9(^3\pi\pi^*/{}^7F_1)$ up to 317 cm^{-1} (involves an Eu-based $^7F_0 \rightarrow {}^7F_1$ transition), compared with those of the free ligands (0.9−9.0 cm^{-1}, Figure S1). Benefiting from the structural rigidity and enhanced coupling, the ligand-centered singlet $^7(^1\pi\pi^*/{}^7F_0)$ state energetically matches the low-lying sublevel of the ligand-centered triplet state, which is the nonet $^9(^3\pi\pi^*/{}^7F_{0-6})$ state of Eu^{3+}−antenna complexes. As shown in Figure 3a, the $^7(^1\pi\pi^*/{}^7F_0)$ state of the complex is exactly degenerate with its $^9(^3\pi\pi^*/{}^7F_1)$ state in the minimum $^7(^1\pi\pi^*/{}^7F_0)$−Min when the visible-light-initiated complex just moves out of the Franck−Condon region with a 1−2 kcal mol^{-1} energy decrease. Kinetic calculations show that the ISC of $^7(^1\pi\pi^*/{}^7F_0) \rightarrow {}^9(^3\pi\pi^*/{}^7F_1)$ takes place within a picosecond timescale (k_{ISC}: up to 6.2 × 10^{12} s^{-1}). The occurrence of ultrafast ISC allows ligand-centered luminescence to incorporate a considerable triplet component since the emission from $^7(^1\pi\pi^*/{}^7F_0)$−Min becomes a slow process with a nanosecond timescale (Figure 4a). As expected, the SOC component analyses demonstrate that the ligand-centered $^1\pi\pi^*$ state in $^7(^1\pi\pi^*/{}^7F_0)$−Min partially exhibits a singlet state character but mixes with the contribution of a 66% triplet counterpart (Figure 3a). The present computational evidence explains why the ligand-centered fluorescence in the singlet state of $^7(^1\pi\pi^*/{}^7F_0)$−Min largely acts as a phosphorescence-like emission with an extremely long lifetime (up to 155 ns). Moreover, the ligand-centered luminescence of **2**−**4** (with a

https://doi.org/10.1021/jacsau.1c00584
JACS Au 2022, 2, 853−864

lifetime of 60−66 ns) appears much earlier than that of **1** (155 ns, Figure 4a) since the introduction of the heavy atom Br in the *para*- or *meta*-position of the phenyl moiety leads to the improvement of the ligand-centered ISC ($^1\pi\pi^* \rightarrow {}^3\pi\pi^*$) rate.

Unlike the triplet-state decay of the isolated ligands (Figure S1), the relatively flat downhill paths instantaneously take the complexes to their nonet-state minima, $^9(^3\pi\pi^*/^7F_0)$−Min. As shown in Figure 3a,c, the $^9(^3\pi\pi^*/^7F_0)$−Min of **1**−**4** was computationally determined to be energetically degenerate with low levels of the corresponding quintet states, $^5(S_0^*/^5D_{0,1})$. This computational evidence suggests that there exists a nonet−quintet crossing NQC($T_1/^7F$−$S_0^*/^5D$) at $^9(^3\pi\pi^*/^7F_0)$−Min, in which the ligand-centered triplet state can relax to its hot ground state (S_0^*), while the released excitation energies promote the ground-state Eu^{3+} to the excited $^5D_{0,1}$ state through 4f electron pairing. The SOC calculations demonstrate that the NQC for complex **1** is composed of 43% nonet and 57% quintet components. Consistently, a two-component regulatory system was experimentally recorded and characterized by the biexponential decay signals of time-resolved luminescence. As illustrated in Figure 4a, typical experimental and fitting results of the biexponential decay data were measured to be located between the ligand-centered (black line) and metal (red line)-centered luminescence at the wavelengths of 536−550 nm (green line) and 581−590 nm (blue line) within the 67−202 and 75−214 ns time regimes, respectively. Computational results show that the two-component signals at the calculated wavelengths of 537−593 nm originate from the phosphorescent emission of the nonet state and the photoluminescence of the $^5D_0$ state under the same minimum structure of the NQC, as shown in Figure 3a,c. To evaluate their efficiencies, the rates for the ligand-centered ISC of $^3\pi\pi^* \rightarrow S_0^*$ were computed to be 2.6×10^6 to 3.4×10^8 s^{-1} for complexes **1**−**4** owing to the relatively small SOC values (Table 1, 0.2−2.2 cm^{-1}) and large energy splitting (Figure 3c, 45.8−53.2 kcal mol^{-1}). The relatively slow rates of the nonradiative processes for the ligand-centered ISC indicate that the lifetimes of the NQC are long enough to trap the Eu−antenna complexes in the minima of the nonet state within timescales of tens to hundreds of nanoseconds.

As shown in Figure 3c and Table 1, there are two types of energy resonances for the ligand-to-metal EnT of lanthanide complexes in the sensitive resonance region arising from the small $^5D_0$−$^5D_1$ splitting of the metal (3.0−4.0 kcal mol^{-1}). The EnT of **1** and **3** proceeds along the energetically matched $^5D_1$ channel, whose f electron pairing takes place in a symmetry-allowed manner ($m_L = +2 \rightarrow m_L = -2$). In contrast, the occurrence of a forbidden $^7F_0 \rightarrow {}^5D_0$ transition ($m_L = +2 \rightarrow m_L = -3$) is mainly responsible for the significant decline in the ligand-to-metal EnT rates of **2** and **4** *via* NQC($T_1/^7F$−$S_0^*/^5D_0$), in which the calculated SOC of $^7F_0 \rightarrow {}^5D_0$ is 1-fold smaller than that of $^7F_0 \rightarrow {}^5D_1$ (Table 1). In the present work, the energetic resonance model is theoretically identified by the energy profiles of the NQC associated with the kinetic assessments of the ligand-centered ISC of $^3\pi\pi^* \rightarrow S_0^*$. Moreover, this theoretical model associated with the operational process of EnT can be further confirmed by the dynamically measured time of ligand-to-metal EnT, which is estimated by the delay time differences between the ligand-centered phosphorescence emission of the nonet state and the photoluminescence of the $^5D_0$ state at the minimum structure of $^9(^3\pi\pi^*/^7F_0)$−Min (*i.e.*, NQC).

Compared with **1**, the nonet state level of **2** slightly decreases and is degenerate with $^5D_0$ of Eu^{3+} instead of the favorable $^5D_1$ channel. In addition to the decreased energy level in the nonet state, the switching of the EnT channel is also attributed to the persistence of the crystal structure and coordination environment around the Eu^{3+} center, which leads to negligible variation in the energy levels of the $^5D_0$ and $^5D_1$ states (Figure 3a). As a consequence, the time of EnT for **2** increases to 28 ns ($^5D_0$) from 12 ns ($^5D_1$) of **1** (Table 1). A 1-fold decrease in the EnT rate is quantitatively correlated with the calculated SOC difference between the $^7F_0 \rightarrow {}^5D_1$ (**1**) and $^7F_0 \rightarrow {}^5D_0$ (**2**) transitions (**1**: 1515 → **2**: 657 cm^{-1}). Although the ligand-centered $^3\pi\pi^* \rightarrow S_0^*$ ISC notably accelerates in the presence of *para*-Br (**1**: 2.6×10^6 to 4.1×10^7 s^{-1} → **2**: 5.9×10^6 to 1.9×10^8 s^{-1}), the ligand-centered excitation energies of **2** are unlikely to transfer smoothly to the Eu^{3+} metal *via* an unfavorable $^5D_0$ channel but release largely through an alternative channel of competitive phosphorescent emission. Consistently, dynamic measurements reveal that the time of phosphorescent emission decreases to 79 ns (**2**) from 202 ns (**1**). An approximate 3-fold increase in phosphorescent emission associated with a more than 1-fold decrease in the ligand-to-metal EnT rate mainly accounts for the decreased quantum yield of metal-centered red luminescence from 69% (**1**) to 55% (**2**) in the presence of the *para*-substituted Br phosphorescence modulator.

As revealed in Figure 3c, the NQCs of **3** and **4** are 8.0−10.0 kcal mol^{-1} energetically lower than those for **1** and **2** in the presence of a *meta*-Br-substituted antenna group, which is mainly attributed to the formation of photostable complexes for **3** and **4** exhibiting a dinuclear structure compared with the 2D layer structure of **1** and **2**. Accordingly, the NQC of **3** is regulated to be located at the optimal level of 19,166 cm^{-1} (54.8 kcal mol^{-1}), allowing the occurrence of ligand-to-metal EnT along a favorable $^5D_1$ channel. Benefiting from the precisely controlled ligand-centered triplet energy and an advantageous channel of intramolecular EnT, the time of EnT for **3** reduces to a minimum value of 6 ns among the four investigated complexes herein (Table 1). The loss of quantum yield arising from the quenching effect in the presence of Eu−H_2O (MeOH) coordination for **3** can be largely compensated by the highly efficient EnT along a favorable $^5D_1$ channel, which produces an acceptable quantum yield of metal-centered red emission (46%). Since the energetic levels of $^5D_{0,1}$ sensitively fluctuate with the coordination microenvironment around the Eu^{3+} center, the attempt to eliminate the drawback of vibrational quenching unexpectedly leads to the EnT channel switching from the favorable $^5D_1$ channel of **3** to the unfavorable $^5D_0$ channel of **4** in the presence of the PNO ligand, resulting in a slightly increased time constant of EnT (8 ns). The introduction of *meta*-Br and PNO ligands significantly narrows the energy splitting (**4**: 45.8 kcal mol^{-1} *vs* **1**−**3**: 51.3−53.2 kcal mol^{-1}) with the enhanced SOC between the ligand-centered $^3\pi\pi^*$ and the corresponding hot ground (S_0^*) states. As a result of regulation in the NQC region, the rate of the ligand-centered ISC for **4** reaches the maximum values (6.3×10^6 to 3.4×10^8 s^{-1}) compared with those of **1**−**3**. On the other hand, however, the time constants of competitive fluorescence (60−65 ns) and phosphorescent (67−79 ns) emissions for **2**−**4** are considerably accelerated by 2−3-fold compared with that of **1** (Flu.: 155 ns, Phos.: 202 ns). This acceleration is mainly due to the enhanced spin−orbit interaction and the decreased energy splitting imposed by

https://doi.org/10.1021/jacsau.1c00584
JACS Au 2022, 2, 853−864

the relativistic effect of the Br heavy atom. The increased radiative rate of the ligand-centered luminescence undesirably contributes an external funnel of excitation energy, thereby reducing the metal-centered emission. This explains why the quantum yield of the metal-centered red emission of **4** (56%) is still lower than that of **1** (69%), although the rate of ligand-to-metal EnT controlled by the ligand-centered ISC has been accelerated considerably. It should be noted that the forward EnT from the ligand to metal is quantitatively characterized by the barrierless paths (see Figure 3), in which the ligand-centered SOC ($^3\pi\pi^* \rightarrow S_0$) acts as the most important controlling factor. By contrast, the occurrence of back-EnT from the metal to ligand encounters small barriers (**1**: 2.6 kcal mol^{-1}, **2**: 0.2 kcal mol^{-1}, **3**: 3.8 kcal mol^{-1}, **4**: 0.3 kcal mol^{-1}), which ensures the efficiencies for the ligand-to-metal EnT and subsequent emission from Eu^{3+} in the repeated forward−backward EnT cycles. Our model differs from the case proposed by Hatanaka and co-workers[53−55] in which the reasonable barriers (instead of SOCs) separately control the dynamics of ligand-to-metal EnT and the ligand-centered ISC in the relaxation paths of terbium(III) complexes.

Rigidity-related excitation-state behaviors of complexes **1**−**4** are further inspected by the transient mid-IR spectra, which have been measured dynamically within the time delay of 0−100 ps (Figure S8). Two characteristic vibrational bands of 1550−1650 and 1650−1750 cm^{-1} were monitored experimentally and confirmed theoretically to originate from the twisting vibrational components of the benzene or pyridine rings and the C═O group in the diketone center, respectively. The visible-light-initiated extra-vibrational signals progressively weaken (benzene or pyridine rings) or disappear totally (C═O) from complexes **1** to **4** within the same timescale (Figure S8) and fit dynamically to the biexponential decay that can be assigned theoretically to the excitation-state relaxations of ligand-centered singlet (fast) and triplet (slow) states, respectively (Figure S8e). The transient mid-IR data clearly demonstrate that with the rigidity enhancement from **1**, **2**, to **4**, the excitation-state energy relaxations become more effective (Figure S8e: up to a more than 1-fold decrease in the decay time). Moreover, the rigidity enhancement of **4** causes a significant decrease in the vibrational contribution for the excited-state nonradiative deactivation, showing a noticeable quantum yield of emission along an unfavorable EnT path ($^5D_0$).

Similar to the quenching effect in the Eu^{3+}−H_2O/CH_3OH coordination, the unrestricted OH vibration largely inhibits the excitation-state energy relaxation of **3**, showing a relatively long decay time (τ_1 = 3.69 ps, τ_2 = 22.32 ps). Moreover, the combined transient mid-IR and luminescence spectra reveal that the most rigid dinuclear complex **4** not only facilitates excitation-state energy relaxation (τ_1 = 0.79 ps and τ_2 = 12.58 ps) but also significantly accelerates the rate of ligand-to-metal EnT (Figure S8e). As shown by the streak camera measurements (Figure 4b), the biexponential decay of luminescence at 500−600 nm for **4** totally disappears in the time delay of 50 ns, but these dynamic signals can still be observed at 1 μs in **1**−**3**, demonstrating an extremely high efficiency of ligand-to-metal EnT for the most rigid **4** (Figure 4b). However, the undesirable ligand-centered luminescence (400−500 nm) of **4** is enhanced simultaneously, and its intensity is 2−3-fold stronger than that its counterparts **1**−**3** at a time delay of 1 μs (Figure 4b). The increased excitation energies funneling from the competitive channel and the coexistent duration of ligand-dependent deactivation greatly reduce the quantum yield of metal-centered red luminescence for **4**.

Taken together, the present computational results and dynamic data suggest that intramolecular EnT-driven lanthanide luminescence is a very complicated photophysical process with multifactor coupling interactive effects. The sensitivity of EnT inherently originates from the existence of symmetry-allowed and symmetry-forbidden channels in the narrowed energy resonance region for some special lanthanide ions, such as Eu^{3+}, bearing a small energy splitting among the metal-centered sublevels (for instance, the energy gap of $^5D_1$−$^5D_0$ is 3−5 kcal mol^{-1} for Eu^{3+}). It has been shown theoretically and verified experimentally that the variation in the luminescence quantum yield controlled by the NQC is a result of the bifurcation into the fast ($^5D_1$) and slow ($^5D_0$) EnT channels, as well as the tunable ligand-centered SOC. Structural comparisons reveal that there are no principal differences in the donor−acceptor distance along the EnT and radiative paths of **1**−**4**, which can be confirmed by the Eu−O distances of the crystal structures (Table S4) and the optimized stationary points (Figures S19−S22). A combination of experimental and computational results indicates that the intramolecular EnT of lanthanide complexes proceeds in an energy-dependent fashion beyond the distance-dependent Förster or Dexter EnT model.

The possible distance dependence *via* a Dexter mechanism for these europium(III) coordination complexes was also examined by employing the strategies developed by our group for treating the photosensitization phenomena of materials and catalytic systems.[56,57] However, extremely small coupling constants were obtained for the coupling terms of Dexter electron exchange, which originates from the weak overlap between the emission spectrum of the ligand and the Eu^{3+} spectrum. In addition, these photoluminescent systems bear the same magnitude of the donor−acceptor distance between the coordinated ligands and Eu^{3+} center. All computational results demonstrate that the distance-dependent models are unlikely to explain the sensitive variation in quantum yield for metal-centered red emission. Based on the multidisciplinary evidence, we can unambiguously conclude that the crossing-controlled EnT model is predominant over the donor−acceptor distance-dependent Förster or Dexter EnT model in the energy degeneracy region. Practical strategies not only require a careful ligand design to strike a delicate balance between the energy level and the spin−orbit interaction for the ligand-centered $^3\pi\pi^*$ toward the $^5D_1/^5D_0$ states of metal and the ligand-centered hot ground state (S_0^*) but also need to establish compromises among the luminescence of the metal, the competitive ligand-centered emission, and the uncontrolled vibrational quenching with vibronic coupling arising from the coordination microenvironment with solvent molecules. This novel crossing-controlled model would be applicable to analogous lanthanide complexes and some representative organic systems, especially when Förster or Dexter EnT models become invalid. This means that once the photo-activated systems evolve into the energy-degenerated crossing, the energy resonance EnT model will be predominant over the donor−acceptor distance-dependent mechanisms and act like an energetically related resonant manner beyond the classical Förster or Dexter EnT models. In our proposed model, the introduction of ligand-centered phosphorescence modulators, which simultaneously improve the ligand-centered ISC and the subsequent ligand-to-metal EnT rate, play a key role in regulating the photoluminescence performance of lanthanide

https://doi.org/10.1021/jacsau.1c00584
JACS Au 2022, 2, 853−864

complexes. We envisioned that numerous studies will be inspired by this design principle to achieve highly efficient light-emitting materials.

CONCLUSIONS

In summary, an innovative model of energy-degeneracy-crossing-controlled EnT has been theoretically determined and experimentally confirmed by using the multiconfigurational second-order perturbation theory, photoluminescence-mechanism-based crystal engineering, and time-resolved spectroscopy. The newly emerged model evaluates the dynamic behaviors of ligand-to-metal EnT related to multifactor coupling interactive photoluminescence for lanthanide complexes as comprehensively as possible. By using this model, many confusing issues will be clarified along the ligand-to-metal EnT and radiative paths of lanthanide complexes and the related systems, that is, the sensitive fluctuation of the quantum yield for metal-centered luminescence with the energy level of the ligand-centered triplet state, the good compromise between the excitation energies funneling from the competitive channel, and the coexistent duration of ligand-dependent deactivation and metal-centered emission, as well as the selection-rule-controlled EnT channel. All this evidence reveals that once the photoactivated systems evolve into the energy degeneracy crossing, the energy resonance EnT model becomes predominant over the donor−acceptor distance-dependent Förster or Dexter mechanisms.

ASSOCIATED CONTENT

Supporting Information

The Supporting Information is available free of charge at https://pubs.acs.org/doi/10.1021/jacsau.1c00584.

Computational mechanism-based design for the candidate antennas, synthesis and characterization of the ligand and Eu-complexes, and computational details (PDF)

AUTHOR INFORMATION

Corresponding Authors

Hao-Ling Sun − *Key Laboratory of Theoretical and Computational Photochemistry of the Ministry of Education, Department of Chemistry, Beijing Normal University, Beijing 100875, China;* orcid.org/0000-0002-2112-4331; Email: haolingsun@bnu.edu.cn

Yunliang Li − *Beijing National Laboratory for Condensed Matter Physics, Institute of Physics, Chinese Academy of Sciences, Beijing 100190, China; School of Physical Sciences, University of Chinese Academy of Sciences, Beijing 100049, China; Songshan Lake Materials Laboratory, Dongguan, Guangdong 523808, China;* orcid.org/0000-0002-5993-2721; Email: yunliangli@iphy.ac.cn

Xuebo Chen − *Key Laboratory of Theoretical and Computational Photochemistry of the Ministry of Education, Department of Chemistry, Beijing Normal University, Beijing 100875, China; College of Chemistry, Zhengzhou University, Zhengzhou, Henan 450001, China;* orcid.org/0000-0002-9814-9908; Email: xuebochen@bnu.edu.cn

Authors

Liangliang Wu − *Key Laboratory of Theoretical and Computational Photochemistry of the Ministry of Education, Department of Chemistry, Beijing Normal University, Beijing 100875, China;* orcid.org/0000-0002-5434-0786

Yu Fang − *Key Laboratory of Theoretical and Computational Photochemistry of the Ministry of Education, Department of Chemistry, Beijing Normal University, Beijing 100875, China*

Wanlong Zuo − *Beijing National Laboratory for Condensed Matter Physics, Institute of Physics, Chinese Academy of Sciences, Beijing 100190, China; College of Physics and Electric Information, Anhui Normal University, Wuhu 241000, China*

Juanjuan Wang − *Key Laboratory of Theoretical and Computational Photochemistry of the Ministry of Education, Department of Chemistry, Beijing Normal University, Beijing 100875, China*

Ju Wang − *State Key Laboratory for Artificial Microstructure and Mesoscopic Physics, Department of Physics, Peking University, Beijing 100871, China*

Shufeng Wang − *State Key Laboratory for Artificial Microstructure and Mesoscopic Physics, Department of Physics, Peking University, Beijing 100871, China;* orcid.org/0000-0003-3536-8000

Zhifeng Cui − *College of Physics and Electric Information, Anhui Normal University, Wuhu 241000, China*

Weihai Fang − *Key Laboratory of Theoretical and Computational Photochemistry of the Ministry of Education, Department of Chemistry, Beijing Normal University, Beijing 100875, China;* orcid.org/0000-0002-1668-465X

Complete contact information is available at: https://pubs.acs.org/10.1021/jacsau.1c00584

Author Contributions

X.C. and W.F. designed the experiments and guided the project. L.W., J.W., and X.C. performed theoretical calculations of the radiative and EnT paths and made the assignments of optical properties for the absorption−emission spectra and the time-resolved spectroscopies. H.S. and Y.F. synthesized the antenna ligands and Eu-complexes and performed the X-ray crystallography and physical measurements. Y.L., W.Z., J.W., S.W., and Z.C. performed the optical measurements and analyzed the dynamic data. All of the authors were involved in the analyses and interpretation of data. X.C. wrote the paper, with help from the coauthors.

Notes

The authors declare no competing financial interest.

ACKNOWLEDGMENTS

For the financial support of this research, we are grateful to the National Natural Science Foundation of China (NSFC21725303, 22120102005, and 22073111) and the National Key Research and Development Projects of China (2016YFA0202300).

REFERENCES

(1) Inanaga, J.; Furuno, H.; Hayano, T. Asymmetric catalysis and amplification with chiral lanthanide complexes. *Chem. Rev.* **2002**, *102*, 2211−2226.

(2) Mikami, K.; Terada, M.; Matsuzawa, H. "Asymmetric" catalysis by lanthanide complexes. *Angew. Chem., Int. Ed.* **2002**, *41*, 3554−3572.

(3) Zheng, W.; Huang, P.; Tu, D.; Ma, E.; Zhu, H.; Chen, X. Lanthanide-doped upconversion nano-bioprobes: electronic struc-

tures, optical properties, and biodetection. *Chem. Soc. Rev.* **2015**, *44*, 1379−1415.
(4) Kido, J.; Okamoto, Y. Organo lanthanide metal complexes for electroluminescent materials. *Chem. Rev.* **2002**, *102*, 2357−2368.
(5) Xu, H.; Sun, Q.; An, Z.; Wei, Y.; Liu, X. Electroluminescence from europium(III) complexes. *Coord. Chem. Rev.* **2015**, *293*−*294*, 228−249.
(6) Feng, J.; Zhang, H. Hybrid materials based on lanthanide organic complexes: a review. *Chem. Soc. Rev.* **2013**, *42*, 387−410.
(7) Binnemans, K. Lanthanide-based luminescent hybrid materials. *Chem. Rev.* **2009**, *109*, 4283−4374.
(8) Dossantos, C.; Harte, A.; Quinn, S.; Gunnlaugsson, T. Recent developments in the field of supramolecular lanthanide luminescent sensors and self-assemblies. *Coord. Chem. Rev.* **2008**, *252*, 2512−2527.
(9) Eliseeva, S. V.; Bünzli, J.-C. G. Lanthanide luminescence for functional materials and bio-sciences. *Chem. Soc. Rev.* **2010**, *39*, 189−227.
(10) Bünzli, J.-C. G. Lanthanide luminescence for biomedical analyses and imaging. *Chem. Res.* **2010**, *110*, 2729−2755.
(11) Debroye, E.; Parac-Vogt, T. N. Towards polymetallic lanthanide complexes as dual contrast agents for magnetic resonance and optical imaging. *Chem. Soc. Rev.* **2014**, *43*, 8178−8192.
(12) Aime, S.; Castelli, D. D.; Crich, S. G.; Gianolio, E.; Terreno, E. Pushing the sensitivity envelope of lanthanide-based magnetic resonance imaging (MRI) contrast agents for molecular imaging applications. *Acc. Chem. Res.* **2009**, *42*, 822−831.
(13) Montgomery, C. P.; Murray, B. S.; New, E. J.; Pal, R.; Parker, D. Cell-penetrating metal complex optical probes: targeted and responsive systems based on lanthanide luminescence. *Acc. Chem. Res.* **2009**, *42*, 925−937.
(14) Heffern, M. C.; Matosziuk, L. M.; Meade, T. J. Lanthanide probes for bioresponsive imaging. *Chem. Rev.* **2014**, *114*, 4496−4539.
(15) Amoroso, A. J.; Pope, S. J. A. Using lanthanide ions in molecular bioimaging. *Chem. Soc. Rev.* **2015**, *44*, 4723−4742.
(16) Minaev, B. F. Effect of spin-orbital interaction on the probability of microwave transitions in a zero field for the phosphorescent state of nitrite ion. *Opt. Spectrosc.* **1977**, *42*, 631−634.
(17) Minaev, B. F. Problem of the Stark effect in spectra of phosphorescent-microwave double resonance. *Opt. Spectrosc.* **1981**, *50*, 209−210.
(18) Minaev, B. F.; Serebrennikov, Y. A. Microwave energy transfer between triplet states of molecules under optical spin orientation conditions. *Soviet Phy. J.* **1979**, *22*, 797−799.
(19) Weissman, S. I. Intramolecular energy transfer the fluorescence of complexes of europium. *J. Chem. Phys.* **1942**, *10*, 214−217.
(20) Moore, E. G.; Samuel, A. P. S.; Raymond, K. N. From antenna to assay: lessons learned in lanthanide luminescence. *Acc. Chem. Res.* **2009**, *42*, 542−552.
(21) Bünzli, J.-C. G. On the design of highly luminescent lanthanide complexes. *Coord. Chem. Rev.* **2015**, *293*, 19−47.
(22) Bünzli, J.-C. G. Rising stars in science and technology: luminescent lanthanide materials. *Eur. J. Inorg. Chem.* **2017**, 5058−5063.
(23) Binnemans, K. Interpretation of europium(III) spectra. *Coord. Chem. Rev.* **2015**, *295*, 1−45.
(24) Ward, M. D. Mechanisms of sensitization of lanthanide(III)-based luminescence in transition metal/lanthanide and anthracene/lanthanide dyads. *Coord. Chem. Rev.* **2010**, *254*, 2634−2642.
(25) Sveshnikova, E. B.; Minaev, B. F. Mechanism of the nonradiative $^1\Delta_g$-$^3\Sigma_g^-$ transition in molecular oxygen in solution. *Opt. Spectrosc.* **1983**, *54*, 320−323.
(26) Gordon, I. E.; Kassi, S.; Campargue, A.; Toon, G. C. First identification of the $a^1\Delta_g$-$X^3\Sigma_g^-$ electric quadrupole transitions of oxygen in solar and laboratory spectra. *J. Quant. Spectrosc. Radiat. Transfer* **2010**, *111*, 1174−1183.
(27) Daumann, L. J.; Tatum, D. S.; Snyder, B. E. R.; Ni, C.; Law, G.-l.; Solomon, E. I.; Raymond, K. N. New insights into structure and luminescence of Eu^{III} and Sm^{III} complexes of the 3, 4, 3-LI (1, 2-HOPO) ligand. *J. Am. Chem. Soc.* **2015**, *137*, 2816−2819.
(28) de Sá, G. F.; de Mello Donegá, C.; Simas, A. M.; Longo, R. L.; Santa-Cruz, P. A.; da Silva, E. F. Spectroscopic properties and design of highly luminescent lanthanide coordination complexes. *Coord. Chem. Rev.* **2000**, *196*, 165−195.
(29) Pacold, J. I.; Tatum, D. S.; Seidler, G. T.; Raymond, K. N.; Zhang, X.; Stickrath, A. B.; Mortensen, D. R. Direct observation of 4f intrashell excitation in luminescent Eu complexes by time-resolved X-ray absorption near edge spectroscopy. *J. Am. Chem. Soc.* **2014**, *136*, 4186−4191.
(30) Mara, M. W.; Tatum, D. S.; March, A.-M.; Doumy, G.; Moore, E. G.; Raymond, K. N. Energy transfer from antenna ligand to europium(III) followed using ultrafast optical and X-ray spectroscopy. *J. Am. Chem. Soc.* **2019**, *141*, 11071−11081.
(31) Lima, P. P.; Nobre, S. S.; Freire, R. O.; Júnior, S. A.; Sá Ferreira, R. A.; Pischel, U.; Malta, O. L.; Carlos, L. D. Energy transfer mechanisms in organic−inorganic hybrids incorporating europium-(III): a quantitative assessment by light emission spectroscopy. *J. Phys. Chem. C* **2007**, *111*, 17627−17634.
(32) Hanaoka, K.; Kikuchi, K.; Kobayashi, S.; Nagano, T. Time-resolved long-lived luminescence imaging method employing luminescent lanthanide probes with a new microscopy system. *J. Am. Chem. Soc.* **2007**, *129*, 13502−13509.
(33) Sveshnikova, E. B.; Morina, V. F.; Ermolaev, V. L. Optics and Spectroscopyl, Mechanism of energy transfer from ketones to ions of rare-earth elements. *Opt. Spectrosc.* **1974**, *36*, 725−732.
(34) Sveshnikova, E. B.; Ermolaev, V. L. Inductive-Resonant Theory of Nonradiative Transitions in Lanthanide and Transition Metal Ions. *Opt. Spectrosc.* **2011**, *111*, 34−50.
(35) Mironov, L. Y.; Sveshnikova, E. B.; Ermolaev, V. L. Direct Evidence of Energy Transfer from a Singlet Ligand Level to Lanthanide Ions in Their Diketonate Complexes. *Opt. Spectrosc.* **2015**, *119*, 77−83.
(36) Horrocks, W. D.; Bolender, J. P.; Smith, W. D.; Supkowski, R. M. Photosensitized Near Infrared Luminescence of Ytterbium(III) in Proteins and Complexes Occurs via an Internal Redox Process. *J. Am. Chem. Soc.* **1997**, *119*, 5972−5973.
(37) Beeby, A.; Faulkner, S.; Williams, J. A. G. pH Dependence of the energy transfer mechanism in a phenanthridine-appended ytterbium complex. *J. Chem. Soc., Dalton Trans.* **2002**, 1918−1922.
(38) Tanner, P. A.; Zhou, L.; Duan, C.; Wong, K.-L. Misconceptions in electronic energy transfer: bridging the gap between chemistry and physics. *Chem. Soc. Rev.* **2018**, *47*, 5234−5265.
(39) Zhang, Q.; Wu, L.; Cao, X.; Chen, X.; Fang, W.; Dolg, M. Energy resonance crossing controls the photoluminescence of europium antenna probes. *Angew. Chem., Int. Ed.* **2017**, *56*, 7986−7990.
(40) Dolg, M.; Cao, X. Relativistic pseudopotentials: their development and scope of applications. *Chem. Res.* **2012**, *112*, 403−480.
(41) Frisch, M. J.; et al. *Gaussian 03*, Revision D. 02; Gaussian, Inc.: Wallingford, CT, 2004.
(42) Werner, H.-J.; Knowles, P. J.; Knizia, G.; Manby, F. R.; Schütz, M. *MOLPRO, Version 2012.1, A Package of Ab Initio Programs*, 2012; available via the Internet at: http://www.molpro.net.
(43) Karlström, G.; Lindh, R.; Malmqvist, P.-Å.; Roos, B. O.; Ryde, U.; Veryazov, V.; Widmark, P.-O.; Cossi, M.; Schimmelpfennig, B.; Neogrady, P.; Seijo, L. MOLCAS: a program package for computational chemistry. *Comput. Mater. Sci.* **2003**, *28*, 222−239.
(44) Reddy, M. L. P.; Divya, V.; Pavithran, R. Visible-light sensitized luminescent europium(III)-β-diketonate complexes: bioprobes for cellular imaging. *Dalton Trans.* **2013**, *42*, 15249−15262.
(45) Binnemans, K.; Görller-Walrand, C. Lanthanide-containing liquid crystals and surfactants. *Chem. Rev.* **2002**, *102*, 2303−2346.
(46) Sato, S.; Wada, M. Relations between Intramolecular energy transfer efficiencies and triplet state energies in rare earth β-diketone chelates. *Bull. Chem. Soc. Jpn.* **1970**, *43*, 1955−1962.
(47) Bünzli, J. C. G.; Eliseeva, S. V. Photophysics of lanthanoid coordination compounds. *Comprehensive Inorganic Chemistry II: From Elements to Applications*, 2nd ed.; Elsevier, 2013; Vol. *8*, pp 339−398.

https://doi.org/10.1021/jacsau.1c00584
JACS Au 2022, 2, 853−864

(48) Ambili Raj, D. B.; Biju, S.; Reddy, M. L. One-, two-, and three-dimensional arrays of Eu^{3+}-4,4,5,5,5-pentafluoro-1-(naphthalen-2-yl)-pentane-1,3-dione complexes: synthesis, crystal structure and photophysical properties. *Inorg. Chem.* **2008**, *47*, 8091.
(49) Jia, L.; Sun, H.-L.; Wang, Z. Crystal structures and luminescent properties of new lanthanide(III) complexes derived from 2-phenyl-4-pyrimidinecarboxylate. *RSC Adv.* **2015**, *5*, 96855−96861.
(50) Jia, L.; Hui, Y.-C.; Li, Z.; Sun, H.-L.; Wang, Z. Luminescent lanthanide-2-phenylpyrimidinecarboxylate frameworks: structure and luminescence tuning. *CrystEngComm* **2014**, *16*, 6483−6490.
(51) He, P.; Wang, H. H.; Liu, S. G.; Shi, J. X.; Wang, G.; Gong, M. L. Visible-light excitable Europium(III) complexes with 2,7-positional substituted carbazole group-containing ligands. *Inorg. Chem.* **2009**, *48*, 11382−11387.
(52) Werts, M. H. V.; Jukes, R. T. F.; Verhoeven, J. W. The emission spectrum and the radiative lifetime of Eu^{3+} in luminescent lanthanide complexes. *Phys. Chem. Chem. Phys.* **2002**, *4*, 1542−1548.
(53) Hatanaka, M.; Morokuma, K. Exploring the Reaction Coordinates for f−f Emission and Quenching of Lanthanide Complexes−Thermosensitivity of Terbium(III) Luminescence. *J. Chem. Theory Comput.* **2014**, *10*, 4184−4188.
(54) Hatanaka, M.; Hirai, Y.; Kitagawa, Y.; Nakanishi, T.; Hasegawa, Y.; Morokuma, K. Organic linkers control the thermosensitivity of the emission intensities from Tb(III) and Eu(III) in a chameleon polymer. *Chem. Sci.* **2017**, *8*, 423−429.
(55) Hatanaka, M.; Osawa, A.; Wakabayashi, T.; Morokuma, K.; Hasegawa, M. Computational study on the luminescence quantum yields of terbium complexes with 2,2′-bipyridine derivative ligands. *Phys. Chem. Chem. Phys.* **2018**, *20*, 3328−3333.
(56) Ma, L.; Fang, W.-H.; Shen, L.; Chen, X. Regulatory mechanism and kinetic assessment of energy transfer catalysis mediated by visible light. *ACS Catal.* **2019**, *9*, 3672−3684.
(57) Han, J.; Shen, L.; Chen, X.; Fang, W. Phosphorescent mechanism for single-dopant white OLED of FPt: electronic structure and electron exchange-induced energy transfer. *J. Mater. Chem. C* **2013**, *1*, 4227−4235.

https://doi.org/10.1021/jacsau.1c00584
JACS Au 2022, 2, 853−864